Evaluating the surface circulation in Ebro Delta (NE Spain) with quality-controlled High Frequency radar measurements

P. Lorente[1], S. Piedracoba[2], J. Soto-Navarro[1] and E. Alvarez-Fanjul[1]

[1]{Puertos del Estado, Avenida del Partenón 10, 28042, Madrid, Spain}

[2]{University of Vigo, Marcosende s/n, 36310, Vigo, Pontevedra, Spain}

Correspondence to: P. Lorente (plorente@puertos.es)

Abstract

Ebro River Delta is a relevant marine protected area in the western Mediterranean. In order to promote the conservation of its ecosystem and support operational decision making in this sensitive area, a three site standard-range (13.5 MHz) CODAR SeaSonde High Frequency (HF) radar was deployed in December 2013. The main goal of this work is to explore basic features of the sea surface circulation in Ebro deltaic region as derived from reliable HF radar surface current measurements. To this aim, a combined quality control methodology was applied: firstly, one year-long (2014) real-time web monitoring of nonvelocity-based diagnostic parameters was conducted to infer both radar site status and HF radar system performance. Signal-to-noise ratio at the monopole exhibited a consistent monthly evolution although some abrupt decreases (below 10 dB), occasionally detected in June for one of the radar sites, impacted negatively on the spatiotemporal coverage of total current vectors. It seemed to be sporadic episodes since radar site overall performance was found to be robust during 2014. Secondly, a validation of HF radar data with independent *in situ* observations from a moored current meter was attempted for May-October 2014. The accuracy assessment of radial and total vectors revealed a consistently high agreement. The directional accuracy of the HF radar was rated at better than 8º. The correlation coefficient and RMSE values emerged in the ranges [0.58-0.83] and [4.02-18.31] $cm \cdot s^{-1}$, respectively. The analysis of the monthly averaged current maps for 2014 showed that the HF radar properly represented basic oceanographic features previously reported, namely: the predominant southwestward flow, the coastal clockwise eddy confined south of Ebro Delta mouth or the Ebro River impulsive-type freshwater discharge. The EOF analysis related the flow response to local wind forcing and confirmed that the surface current field evolved in space and time according to three significantly dominant modes of variability.

1. Introduction.

The circulation in Ebro continental margin (NE Spain, Fig. 1 - a) is mainly thermohaline and characterized by a quasi-permanent barotropic shelf-slope jet, which flows southwestwards and is named 'the North current', only altered by clockwise inertial oscillations and some short periods of current reversals. This relatively low-intensity current flow (10 $cm \cdot s^{-1}$) is in geostrophic balance with the so-called Catalan front, which is a permanent density front associated with strong salinity gradients maintained by the Ebro River runoff (Font *et al*., 1988a).

The marine circulation near the delta, although dominated by the alongshore large-scale dynamics, presents a complex structure strongly influenced by the topography, the seasonality of the remarkable Ebro River discharges (Font *et al*., 1988b), the changing wind conditions and the water column thermal stratification (Salat *et al*., 2002). Nonetheless, the tidal influence in the continental shelf currents field is very weak as expected for a microtidal and low-energy environment (Jimenez *et al*., 2002).

Since the Ebro River Delta is one of the most relevant marine protected areas in the western Mediterranean in terms of biodiversity, an intense monitoring activity is performed to manage this deltaic coastal region and promote the conservation of its ecosystem. In order to support marine domain awareness and operational decision making in this sensitive area, a network of 13.5 MHz CODAR SeaSonde High Frequency (HF) radar systems has been deployed (Fig. 1 - b). HF radar has been steadily gaining recognition as an efficient land-based remote sensing instrument for mapping surface currents at high spatial and temporal resolutions in near real time. This technology presents a broad range of practical applications, encompassing management (SAR operations, oil spill emergencies), commercial (vessel tracking, ocean energy production) and research (ecology, water quality, fisheries) uses. Other emerging uses include the validation of operational ocean forecasting systems or assimilation into numerical coastal circulation models (Marmain et al., 2014; Stanev et al., 2015).

As a consequence, there is a growing demand for quality-controlled HF radar surface current measurements. Since HF radar estimations are subject to many potential uncertainties (namely: power-line disturbances, radio frequency interferences, ionosphere clutter, ship echoes, antenna pattern distortions or environmental noise - see Kohut and Glenn, 2003), many efforts have been recently devoted to identify occasional non-realistic radar current vectors. Such artefacts (defined as spikes, spurious values or corrupted data) are generally detected at the outer edges of the radar domain and flagged in accordance with a pre-defined protocol. An individual quality control (QC) index, based on an integer number derived from a battery of tests, should be assigned for each and every single radar grid-cell to indicate the quality level of each measured value (Gomez *et al*., 2015).

The artefacts can be subsequently eliminated from the data stream in real time (Cosoli *et al*., 2012b) or offline (Liu *et al*, 2014). Other approaches are focused, in addition, on replacing noisy values with more reliable estimates (Wyatt *et al*., 2015) by using open-boundary model analysis (Kaplan and Lekien, 2007) or statistical mapping (Barrick *et al*., 2012). However, the main drawback lies with the potential removal of accurate data when the discriminating algorithm is based on tight thresholds. Some fine-tuning, based on the specific local conditions of the system, is thus required to have the right trade-off between

confirmed outlier identification and false alarm rate, maximizing the benefit of the applications of these methods (Gomez *et al*., 2014).

Whereas some quality indexes are assigned according to velocity-based QC schemes, other approaches intend to use nonvelocity-based metrics related to the characteristics of the received signal in order to implement advanced quality controls and reduce the systematic errors in radar current estimates (Kirincich et al., 2002). One of the radial metrics that offers the most potential benefits as reliability indicator is the Signal-to-Noise Ratio of sea-echo at the monopole (SNR3), since it has been previously proved to be a valid proxy for both radar site status and onset of HF radar system malfunction (Cosoli et al., 2012b; Roarty et al., 2012). Complementarily, a big jump in the average state over time in antenna parameters (*e.g*. amplitude corrections for loops 1 and 2 to the monopole, AMP1 and AMP2, respectively) may indicate an antenna problem and should be investigated (COS, 2005).

In this context, a number of previous works have focused on defining optimum threshold levels since there is still no worldwide consensus. Atwater and Heron (2011) showed that a simple thresholding of SNR3 is a good starting point, although a 20 dB limit constitutes a too severe QC criterion with a resulting detrimental impact on coverage area. Values of SNR3 below 10 dB have been proved to be closely linked to a significant decrease of the Multiple Signal Characterization (MUSIC) direction-finding algorithm skill (De Paolo and Terril, 2007). As MUSIC is employed to resolve ocean surface current structure (Schmidt, 1986), limitations in its performance are related to potentially suspect velocity outputs. Furthermore, different combinations of dynamic thresholds cutoffs have been analyzed to quantify the potential for error reduction (De Paolo *et al*., 2015). Since the question still remains open, further researches are currently underway to shed light on it.

In addition, the credibility of HF radar data has been previously tested in extensive validation studies, including direct comparisons of HF radar-derived surface currents against independent in situ sensors like moored ADCP's, point-wise current meters – PCM hereinafter-, drifters or similar (Graber *et al*., 1997; Kaplan *et al*., 2005; Cosoli *et al*., 2010; Solabarrieta et al., 2014). Accordingly, a number of accuracy assessment exercises have been performed with the HF coastal radar network operated by Puertos del Estado (Fig. 1 – a) -PdE hereinafter- in order to quantify and lower uncertainties in radar current measurements (Alfonso *et al*., 2006; Lorente *et al*., 2014, 2015a and 2015b).

Correlation coefficients (CORR) and root mean squared errors (RMSE) have been previously found to be in the ranges [0.32-0.92] and [6-30 $cm \cdot s^{-1}$], respectively (Kohut and Glenn 2003; Paduan *et al*., 2006; Chapman and Graber, 1997). Relative HF radar velocity errors can vary dramatically with the radar transmission frequency, sensor type and location within the sampled domain, as well as the data processing scheme used (Rypina *et al*., 2014; Kirincich *et al*., 2012). In this frame, the instrumental noise and sub-grid scale current variability have been reported to yield noise levels of 4-6 $cm \cdot s^{-1}$ (Emery *et al*., 2004; Ohlmann *et al*., 2007; De Paolo *et al*., 2015).

The main goal of this work is to explore basic features of the sea surface circulation in Ebro River Delta as derived from reliable and accurate HF radar surface current measurements. To this aim, a combined QC methodology is firstly applied: one year-long real-time web monitoring of nonvelocity-based diagnostic parameters and offline validation

of HF radar-derived current data with *in situ* observations from a PCM installed in a buoy moored within the radar domain (B1, Fig. 1 - b). This integrated approach is used during 2014 in order to infer both radar site status and HF radar system overall performance and also to provide upper bounds on both radial and total radar current measurement accuracy (Lorente *et al.*, 2015c). Once HF radar data quality is estimated, Ebro Delta HF radar capabilities in reproducing well-known circulation features are investigated through the exploration of monthly averaged flow patterns and dominant modes of variability both in time and space (Cosoli *et al.*, 2012a and 2013; Kovacevik *et al.*, 2004). Lastly, the relative contribution of local wind as forcing mechanism is evaluated.

This paper is organized as follows: sections 2 and 3 outline the specific instrumentation and methods used in this study, respectively, followed in section 4 by a detailed discussion of the results. Finally, main conclusions are summarized in section 5.

2. Instrumentation.

2.1. HF radar.

A CODAR SeaSonde standard-range HF radar system was deployed at Ebro Delta in December 2013 within the frame of RIADE (Redes de Indicadores Ambientales del Delta del Ebro) project. The HF radar network consists of an array of three remote shore-based sites: Salou, Vinaroz and Alfacada. They will hereafter be referred to by their four letter site codes: SALO, VINA and ALFA, respectively (Fig. 1 - b).

The HF radar technology, founded on principle of Bragg scattering of the electromagnetic radiation over a rough sea (Crombie, 1955), infer the radial current component from the Doppler-shift of radio waves back-scattered by surface gravity waves of half their electromagnetic wavelength. Each single radar site is configured to estimate radial currents moving toward or away from the receive antenna. Since the speed of the wave is easily derived from linear wave theory, the velocity of the underlying ocean surface currents can be computed by subtraction. The distance to the backscattered signal is determined by range-gating the returns and the angle of origin is inferred, in the case of CODAR SeaSonde radars, by a direction-finding process (Barrick and Lipa, 1986) using three collocated receive antennas (two orthogonal crossed loops and a single monopole) and the MUSIC algorithm (Schmidt, 1986).

Each site is operating at a nominal frequency of 13.5 MHz with a 90 KHz bandwidth, providing hourly radial measurements with a cut-off filter of 100 $cm \cdot s^{-1}$ and representative of current velocities in the upper first meter of the water column. Only calibrated (measured) antenna beam patterns (hereinafter APM) were employed by the manufacturer supplied software to process radial data used in the present study, with the aim of maximizing HF radar usefulness for operational applications (Lipa *et al.*, 2006; Kohut and Glenn, 2003). In regions of overlapping coverage from two or more sites, radial current measurements are geometrically combined using a least-square fit technique (Barrick and Lipa, 1986) with the averaging radius set to 6 km in order to estimate hourly averaged total current vectors on a predefined Cartesian regular grid with 3 x 3 km horizontal resolution. The maximum horizontal range is set to 80 km and the angular resolution is 5º.

HF radar-derived data used in this study have been collected from 1 January to 31 December 2014 (Fig. 1 - c). During this period the three sites were simultaneously operational and radar coverage was as its maximum extent. Temporal data coverage was quantified by computing the percent of total possible vector returns at each radar grid point (Fig. 1 - b). Percent coverage decreases rapidly near the outer edges of the domain where error levels are higher due to poor intersecting beam geometry (Chapman and Graber, 1997) and quantified by larger Geometric Dilution of Precision (GDOP, Chapman *et al*, 1997). GDOP is an unit-less coefficient of uncertainty that characterizes how radar geometry may impact on measurement accuracy and position determination errors, owing to the angle at which the radials intersect and also to uncertainties in the radial vectors geometrically combined (Levanon, 2000; Trujillo *et al*., 2004).

With the aim of screening out radar grid points where data are less reliable, a threshold on percent coverage has been imposed. Only time series of zonal and meridional surface currents at grid points with percent coverage greater than 50% over the 2014 annual record have been considered in this study. The selected coverage area present associated GDOP values of 1.5 or less.

2.2. Buoy B1.

The domain of Ebro Delta HF radar array includes an ocean Seawatch buoy deployed since August 2004 in the eastern waters of the Iberian Peninsula: Tarragona buoy (40.68ºN, 1.47ºE, 688 meters depth), hereafter referred to as B1 (Fig. 1 - b). This buoy is equipped with an acoustic point-wise current meter manufactured by Falmouth Scientific Inc., providing quality-controlled hourly averaged current velocity vectors at a nominal depth of three meters. A wind speed and direction sensor manufactured by R. M. Young Company measures hourly wind data at a nominal height of 3 meters. It should be noted that current and wind records are only available from 1 May to 31 October, 2014 (Fig. 1 - c). B1 suffered from brief communication outages during this period and subsequent short gaps (2-3 h) in data time series have been linearly interpolated.

3. Methods.

3.1. Online Quality Control of HF radar measurements.

In order to ensure the reliability of the HF radar products delivered, maintenance and Quality Control (QC) procedures must be performed at various stages on the data generation pipeline. The manufacturer software package integrates a set of QC routines and thresholding techniques in the data processing chain (*e.g*., limits for maximum vector magnitude and maximum GDOP).

This section presents a simplistic approach based on additional data quality checks at the post-processing stage and devoted to examine a variety of nonvelocity-based diagnostic parameters provided by the manufacturer (CODAR Ocean Sensors -COS-) and listed in Table 1. Such indicators include hardware, antenna, radial and total parameters, employed here as diagnostic tools for evaluating HF radar integrity and health (Roarty *et al*., 2012, Emery and Washburn, 2007). A dedicated online website has been developed to operationally monitor in real time radar site status since anomalous values, inconsistencies

or sharp fluctuations in the indicators might be related to potential malfunctions. This automated quality control web tool runs in background with a cron job, being updated on an hourly basis.

One year-long (2014) real-time monitoring has been performed in order to inspect the temporal evolution and consistency of the aforementioned parameters, obtain estimates of their standard ranges and evaluate Ebro Delta radar site performance according to them (Lorente *et al*., 2015a). Abrupt or gradual degradation and failures can be easily detected, triggering alerts for troubleshooting when defined thresholds (initially set to two standard deviations above/below the mean) are persistently exceeded. Particular emphasis has been devoted to SNR3 and the number of radial vectors provided.

Finally, automated quality checks have been implemented at the second level within the hierarchy defined for QC procedures, referred to total vectors. Temporal and spatial coverage of Ebro Delta radar system are separately analyzed on a monthly basis and later confronted to each other to check if HF radar systems operate within tolerance ranges, fulfilling the recommended level of data provision: 80% of the spatial region over the 80% of the time (Roarty *et al*., 2012).

3.2. HF radar validation.

Since the Ebro Delta HF radar footprint overlooks of a moored PCM within its spatial coverage, an accuracy assessment of radar surface currents is performed for a 6-month period May-October 2014 of concurrent radar-PCM measurements (Fig. 1 - c). The present section builds on previous investigations devoted to the determination of measurements errors, the evaluation of direction-finding capabilities and the angular distribution of radial velocity uncertainties (Emery *et al*., 2004; Paduan *et al*., 2006; Cosoli *et al*., 2010; De Paolo and Terrill, 2007).

To this aim, the radar radial arc geographically closest to B1 buoy location has been selected for each HF radar site and radial current vectors estimated at each arc point have been compared with the radial projection of PCM velocities. The B1-HF radar comparative analysis allows the computation of statistical parameters (*e.g.,* CORR and RMSE) as a function of the angle comprised between B1 and the arc grid point position. In absence of direction-finding errors (DF), maximum CORR and minimum RMSE values should be found over the arc point closest to B1 location. In presence of DF, the bearing offset is thus expressed as the angular difference between the arc point with maximum correlation and the buoy location.

Radial current time series have been filtered to remove all tidal, diurnal and inertial fluctuations (the inertial period is 18.4 h at B1 location latitude) from the velocity data. Filtered time series, obtained after applying a 10^{th} order digital low-pass Butterworth filter with a cut-off period of 30 h (Emery and Thomson, 2001), have been compared to evaluate the discrepancies in subinertial currents.

Complementarily, HF radar total vector hourly estimations at the grid point closest to B1 location (HFR1, 1.48ºE 40.69ºN, Fig. 1 - b) have been compared with PCM velocities to provide upper bounds on the radar current measurement accuracy. Comparisons have been undertaken using zonal (U) and meridional (V) components in order to evaluate the

agreement between both instruments by means of the computation of a set of statistical metrics – RMSE, scalar and complex correlations and best linear fit of scatter plots. Monthly results have been summarized with Taylor diagrams (Taylor, 2001), which provide a concise statistical summary of the agreement between both datasets.

Finally, rotatory spectral analyses (Gonella, 1972) have been performed for HF radar-derived total vectors at HFR1 location and for current data from B1 in order to identify the dominant modes of temporal variability. To ensure the continuity of the data record, small gaps detected (not larger than 6 h) in time series have been linearly interpolated. Spectra have been calculated by dividing time series into successive six day segments, with a 50% overlap and a Hanning window (Emery and Thompson, 2001), and subsequently averaged to provide some smoothing. Confidence levels for spectra densities have been derived assuming a chi-squared distribution for the variance.

3.3. Characterization of the surface circulation field

Maps of the Eulerian mean current field have been constructed at monthly time scale from the raw (unfiltered) radar time series on a subsampled grid with the aim of assessing the surface current dynamics in Ebro Delta. Additionally, a complex Empirical Orthogonal Function (EOF) decomposition (Kundu and Allen, 1976) has been used to infer the driving forces and spatiotemporal scales behind the variability of sea surface currents (Kaihatu *et al*., 1998). This method, which reduces the components of the vector field to a complex scalar, has become widespread in order to extract the dominant modes of variability. The representative spatial patterns (or EOF modes) and their corresponding temporal coefficients or principal components (PCs, which describe the evolution of the modes) are determined by using the singular value decomposition of the covariance matrix. Each statistically significant EOF mode explains a limited portion of the total surface current variance.

EOF analysis has been applied to radar current velocity dataset using again the raw (unfiltered) hourly time series for the entire year 2014. Main spatial modes obtained for HF radar have been interpreted in terms of physical processes related to the detected spatially coherent structures. Since EOFs are purely statistical, each EOF mode's statistical significance must be evaluated. Several rules of thumb have been previously proposed indicating when an EOF is likely to be subject to large sampling fluctuations. In the present work, error estimates based on temporal decorrelation scales have been calculated according to North et al. (1982):

$$\delta(\lambda_i) = \lambda_i * (2/N)^{\frac{1}{2}} \quad [1]$$

Where δ_i is the eigenvalue for mode i, and N is the number of degrees of freedom determined using a conservative two-day decorrelation time-scale, following Münchow and Chant (2000). If the confidence intervals from the error estimates of any modes overlap, the modes may be non-orthogonal and can not be considered distinct and uncorrelated. Consequently, such modes are excluded from the EOF analysis and hence only the first previous modes can be considered to contain a significant portion of the total variance and to properly reproduce the observed surface current fields.

Finally, hourly wind vector dataset registered at B1 buoy has been also decomposed into principal components in order to infer the main axis of variability. Particular emphasis has been placed on the relationship between wind and radar-derived current EOF modes of variability in order to derive a better statistical insight.

4. Results and discussion

4.1. Annual Quality Control

Box plots of SNR3 for each radar site (Fig. 2 – a, b, c) exhibit a consistent monthly evolution, with a median (central mark) above 40 dB. However, a number of sharp decreases can be occasionally observed in VINA site for the month of June (Fig. 2 - c), exceeding the previously reported threshold of 10 dB (De Paolo and Terril, 2007).

The annual time series of hourly SNR3 values for VINA site (Fig. 2 - d) reveals that the thresholds proposed in the present work (two standard deviations above/below the mean, represented by bold blue dotted lines) were abruptly exceeded several times in June. SNR3 reached extremely low values, leading to a drastic reduction in the radar spatial coverage presumably related to an inherent limitation of MUSIC algorithm, namely, the extraction of a maximum of two bearing solutions for a given range cell and a given radial current velocity. In this context, poor SNR3 values associated with potential interferences or environmental noise can lead to ambiguities in the estimation of the direction of arrival (DOA) function performed by MUSIC algorithm. Such ambiguities, based on the existence of more than two bearing solutions, eventually produce gaps in HF radar spatial coverage since additional solutions are excluded.

Consequently, the number of radial vectors (NRV) provided by VINA lowered significantly in June (Fig. 2 - e). Leaving aside the regular high frequency fluctuations due to the day/night cycle, NRV was several times below 500 and even equal to zero, indicating a poorer than expected performance of VINA site during this month. Nonetheless, it appears to be a sporadic episode, maybe related to radio-wave interferences, since VINA presented a stable performance during the second semester of 2014.

The quality checks implemented at total vectors level allow an overall evaluation of Ebro Delta HF radar system performance on a monthly basis (Fig. 3). A comparative analysis for February and June confirms the degraded performance during the latter. Data availability generally exceeded 80% in time over the majority of the radar footprint in February, with an abrupt decrease at the periphery of the radar range (Fig. 3 - a). By contrast, it only outreached the 50% in June, with a smoother transition at the outer edges of the domain (Fig. 3 – b). The evolution of the spatial coverage was rather consistent in February, with sporadic decreases below 50% (Fig. 3 - c). On the contrary, an irregular performance is detected in June as a consequence of both ALFA site outage (1-8 June) and VINA irregular behavior (Fig. 3 - d). The first factor yielded a dramatic and persistent drop in the areal coverage, lower than 20% most of the time. The second led to a significant, albeit occasional, reduction in the radar spatial domain (below 50%), which can be observed from 8 to 30 June 2014.

Finally, the temporal and spatial coverage have been confronted to each other (Fig. 3 – e, f). Ebro Delta radar system was closer to fulfill the required 80%-80% level of data

provision in February (Roarty *et al*., 2012), with a 64% of the areal domain (referred to its maximum extent) available the 80% of the time. By contrast, the radar system barely reached the 35% of spatial coverage for the 80% of the time in June. Despite this occasional degradation, radar sites overall performance and their day-to-day operation have been found to be robust and within tolerance ranges. One year of continuous operation revealed three sites up and operational in excess of 95% of the time, with sporadic interruptions that introduced short-duration gaps in time and space (Fig. 1 - c).

It is noteworthy that the described methodology, at this preliminary development stage, is not able to remove suspicious values or outliers from the data stream in real time like Cosoli *et al*. (2012b) but only to detect anomalies and categorize them in order to create a historic database of flagged radial files similar to Roarty *et al*. (2012) for a later offline reprocessing of total vector maps when one (or more) radar site(s) is (are) considered to be working abnormally.

In this context, the hourly radial vectors provided by VINA site in June that did not satisfy the proposed QC control have been discarded from the analyses performed in the next sections and the associated total vector maps have been accordingly reprocessed offline. Future efforts should be devoted to improve radial data quality in real-time prior to the vector combination process and also to assign meaningful quality descriptor flags for each grid point data in total current fields.

4.2. Buoy-radar comparison results

The evaluation of direction-finding capabilities revealed the existence of small bearing errors (hereafter $\Delta\alpha$) in radar radial estimations, ranging between 2°-8° (Fig. 4) and in accordance with the typical values previously reported (Emery et al., 2004; Paduan *et al*., 2006). Comparison of unfiltered hourly radial currents estimated by B1 and SALO site (Fig. 4 - b) shows maximum CORR in a grid point (denoted by vertical solid red line) angularly close to B1 location (vertical dotted black line): 0.79, with associated RMSE of 10.95 $cm \cdot s^{-1}$ and $\Delta\alpha$ of 3.74º in the counter-clockwise direction. VINA site (Fig. 4 - c) presents a lower bearing offset ($\Delta\alpha$ = 1.82º) but also lower (higher) CORR (RMSE) value of 0.58 (13.31 $cm \cdot s^{-1}$). It is worth mentioning that minimum RMSE values are also placed on the vicinity of the correlation peaks. The VINA site exhibits the largest pointing error ($\Delta\alpha$ = 7.82º) and the poorest agreement with moored radial estimations as CORR is 0.58 and RMSE is fairly above 18 $cm \cdot s^{-1}$ (Fig. 4 - d).

Hourly time series of low-pass filtered radial currents measured by B1 and those estimated in the closest range arc point (“best match-angle”) by each HF radar site are presented in Fig. 5. Metrics derived from the accuracy assessment highlight the consistently high agreement between SALO radar site and B1 estimations, with a CORR and RMSE values of 0.80 and 5.58 $cm \cdot s^{-1}$, respectively (Fig. 5 - a). Results derived from the best linear fit reveal a slope close to 1 and an intercept up to -0.82 $cm \cdot s^{-1}$. The concordance between ALFA site and B1 is moderately good, with acceptable pairs of values CORR-RMSE and slope-intercept: [0.63-6.91] $cm \cdot s^{-1}$ and [0.73-1.92] $cm \cdot s^{-1}$, respectively (Fig. 5 - b). VINA site data show lower agreement with *in situ* measurements (Fig. 5 - c) as reflected by a lower (higher) CORR (RMSE) value of 0.56 (7.76 $cm \cdot s^{-1}$). This might be partially attributable to the long site-buoy distance (*i.e*., the radar signal is weaker) and to the limited

radar data availability due to day/night coverage fluctuations (*i.e.*, the data return is more than three times lower, with only 986 hourly observations available).

Ancillary validation works with radial measurements like internal self-consistency checks have not been performed due to Ebro Delta radar sites' geometry. Radar-to-radar comparisons along the overwater baselines (Paduan *et al.*, 2006; Yoshikawa *et al.*, 2006; Atwater and Heron, 2010), although valuable to explore quantitatively intrinsic uncertainties in radial velocities, are not feasible since they are positioned over land or near the coastline.

Statistical metrics derived from filtered hourly time series comparison of zonal (U) and meridional (V) components of total vectors estimated by B1 and HFR1 for the 6-month period are presented in Fig. 6. Results reveal a good agreement for both components (CORR above 0.74), in accordance with results reported in the literature (Cosoli *et al.*, 2010; Kaplan *et al.*, 2005). RMSE is significantly higher for the zonal component than the meridional: 12.69 versus 4.02 $cm \cdot s^{-1}$ (Fig. 6 – a, b). The disparity of uncertainty levels between the east and north component vectors comes for the geometry of the radar vector combination and the prevalent south-southwestward current flow. This presumably might lead to less (more) precise radial vectors provided by ALFA (SALO) radar site since radial measurements are proved to be more accurate when the dominant current flow moves in the same direction (Robinson *et al.*, 2011). Since ALFA (SALO) site contributed mainly to the HF radar zonal (meridional) current assessment in B1 nearby region, a strong relationship between radial and total vector uncertainties has been evidenced.

The scatter plots (not shown) and the associated best linear fits show that HF radar slightly underestimates total current velocities registered by B1 since the slopes are below 1: 0.71 and 0.67 for U and V components, respectively. The time-averaged complex correlation coefficient between B1 and HFR1 currents at zero lag is 0.77. The related phase is 8.65º, indicating that the former are, on average, slightly right shifted since the veering angle gives the average counter-clockwise turning of the second vector with respect to the first vector (Kundu, 1976).

The monthly mean current values were computed to characterize the main features of the flow in this region. The descriptive statistics reveal predominant negative values for the zonal speed (Fig. 6 - c) and a quasi-permanent average flow in the N-S direction (Fig. 6 - d). There is no evidence of a seasonal signal in both zonal and meridional velocity components of radar and B1 surface currents. Therefore, both instruments exhibit similar monthly mean values and variability, capturing the well-known southwestward thermohaline flow and identifying episodic but intense current reversals, as those observed by mid-September (Fig. 6 – a, b).

The monthly comparison of total vectors, performed on the unfiltered time series, provide a variety of metrics that are concisely summarized in a Taylor diagram (Taylor, 2001), shown in Fig. 7. The diagram compares both data sets by combining information about their relative standard deviations, centered RMSE and CORR, synthetizing the statistical information of how closely the radar measurements at HFR1 grid point match with B1 velocities. As it can be seen, the cluster of points that show best agreement (*i.e.*, are closest to their corresponding reference point, labeled with blue squares) are those corresponding to the period May-September (red squares, sequentially numbered 1-5). The

reported correlation coefficient, standard deviation and RMSE values emerge in the ranges of [0.72-0.83], [10.96-14.18 $cm \cdot s^{-1}$] and [7.48-8.75 $cm \cdot s^{-1}$], respectively, for both zonal and meridional velocity components (Fig. 7 – a, b). However, HF radar is less accurate by the last month of the analyzed period, since metrics computed for October (red square 6) reflect lower (higher) CORR (RMSE) values: 0.50-0.58 (10.92-11.03).

Instrument-to-instrument comparisons present intrinsic limitations since both devices operate differently and at distinct nominal depths. A fraction of observed radar-B1 differences can thus be explained in terms of different sampling strategies on disparate time and space scales (Ohlmann *et al*., 2007). In this context, many of the uncertainties associated with HF radar technology are geometric in nature. Apart from the instrumental noise, other sources of potential errors in vector currents might be the sub-grid horizontal shear, the geophysical variability within the water column (Graber *et al*, 1997) and some specific processes, namely, the Stokes drift, the Ekman drift and baroclinity (Paduan *et al*., 2006).

Spectral analyses have been computed for a 6-month period May-October 2014 (warm stratified season) to examine power spectral discrepancies in the frequency domain between both instruments. B1 and HFR1 current time series present qualitatively similar characteristics, capturing properly the dominant features within the diurnal and inertial bands, related to significantly prevalent clockwise (CW) rotatory motions (solid lines, Fig. 8). Relevant polarized peaks are evident for both datasets, although their amplitudes are slightly larger for radar currents (solid red line). The inertial peak is the most pronounced, pointing out the adjustment of the stratified fluid to the wind driven currents and, subsequently, the importance of local wind as forcing mechanism (addressed in section 4.3.2). Offshore oscillations in this frequency band are a common feature in ocean circulation and their presence in the study area has been previously documented (Font *et al*., 1990). By contrast, the counter-clockwise component (CCW, dotted lines) is much less energetic (especially in the case of B1 current estimations) and is where the main radar-B1 differences in variance distribution can be found. Finally, a drop of energy and later flattening about 2 cpd are common for the CW components of both B1 and radar spectra, although the latter presents larger energy at that frequency band. Radar surface estimations are influenced by energetic high-frequency processes related to air-sea interaction like highly variable and strong wind gusts, which are not fully contained in sub-surface current estimations provided by the current meter.

4.3. Dominant features of the surface flow

4.3.1. Monthly averaged current patterns

The sequence of monthly averaged current maps in Fig. 9 shows that some of the main circulation features in Ebro Delta remain rather invariant throughout most part of the year, like the southwestward slope jet, associated with the highest velocities detected (above 30 $cm \cdot s^{-1}$). The current speed diminishes toward coastal areas, except in the vicinity of ALFA radar site, where the signal of Ebro River impulsive-type freshwater outflow is clearly evidenced during winter and spring (Fig. 9 - a, b, f). As a consequence of the remarkable seasonal variability of Ebro discharge rates, the river plume loses intensity during the warm

season (Fig. 9 - c), becoming barely noticeable in late summer and early autumn (Fig. 9 – d, e), until the beginning of the following hydrological cycle (Fig. 9 - f).

It is noteworthy the weakening of the southwestward slope jet during the central part of the year, in agreement with reported short periods of current reversals (Font *et al*., 1990). The jet is intensified in October, perhaps as a result of the observed increase of the mesoscale activity (Font *et al*., 1995), reaching ultimately a peak strength in December. By the end of 2014, the monthly spatial patterns become rather uniform, revealing the acceleration of the jet (with a spatial propagation of maximum velocities, exceeding 40 $cm \cdot s^{-1}$) on the eastern region of the radar domain and also the presence of two small-scale coastal meanders (Fig. 9 - e, f).

A coastal anticyclonic eddy can also be observed in radar data, confined south of Ebro Delta mouth (Fig. 9 – a, b, c). This hydrodynamic feature has been well-documented in previous studies (Font et al., 1990; Salat et al., 2002), which stated the interaction of the buoyancy-driven flow with the topography as triggering source of this clockwise gyre, eventually reinforcing the shelf/slope front that drives the general circulation to the south-southwest. In addition, persistent and high-intensity NW wind jets (called 'mistral' winds), dominant during the October-May cold season and channeled by the narrow Ebro Valley, have been reported to introduce negative vorticity in the flow south of the Ebro Delta and reinforce the long-time preservation of this small-scale eddy (Garcia and Ballester, 1984; Espino *et al*., 1998). Notwithstanding, this coastal clockwise rotation is eventually absent from September (not shown) to December monthly averaged current maps.

During the transition month of August, a large anticyclonic recirculation cell is evidenced, detached from the shore and located on the center of radar domain (Fig. 9 - d). This current pattern is dominated by the interaction of the cross-shelf flow on the southern inner shelf with topographic obstacles, giving rise to a shift to the right of the coastal flow. The subsequent northeastward reversal of the inshore flow is scarcely influenced by Ebro River freshwater discharge as it reaches the lowest value at this stage of the year.

4.3.2. Empirical orthogonal function (EOF) analysis

The mean and EOFs of hourly surface currents have been calculated for the entire 2014 (Fig. 10). The long-term mean flow (Fig. 10 - a) captures the main circulation features previously reported about 'the North Current', characterized by a quasi-permanent shelf-slope jet oriented southwestward and a remarkable Ebro River impulsive-type freshwater discharge (located in front of ALFA site). The buoyancy input introduced by large delta outflows, together with topographic effects, lead to the development of the aforementioned anticyclonic coastal eddy on the southern side of the delta.

Since the EOF analysis has been performed on the unfiltered data set containing relevant high-frequency spatiotemporal variability, the first three EOFs cumulatively account only for the 46.1% of the total variance (26.1%, 15.3% and 4.7%, respectively). Only the first three EOF modes are statistically significant according to the mode selection rule and truncation criterion suggested by North et al. (1982). The first, second and third modes are distinct and uncorrelated; however, the fourth mode is not since its error bars overlap with those of mode 5 (not shown). Therefore, higher order modes will not be further addressed

here as they represent a combination of unresolved high-frequency motions or noise (Cosoli *et al.*, 2012a).

The first dominant EOF mode (Fig. 10 - b) represents a spatially uniform pattern, rather similar to the annual averaged current map, with a prevailing alongshore shelf-slope jet flowing mainly southwestward, basically capturing the thermohaline Catalan front. The second EOF (Fig. 10 - c) shows a homogeneous spatial structure, perpendicular to the first mode, with a well-defined offshore-directed flow. The spatial pattern of EOF3 (Fig. 10 - d) adds some complexity to the basic uniform flows represented by the first two modes, since it introduces curvature to the current field by means of a large, albeit weak, anticyclonic recirculation cell (flow divergence) in the central (southern) region of the radar domain.

Temporal variation in the strength of these three EOF modes is represented by their corresponding principal components, shown in Fig. 11. EOF1 is predominantly positive except during the summertime, when the quasi-permanent flow to the SW is altered by clockwise inertial oscillations (positive EOF3) and some periods of current reversals, with maximum occurrence during the stratified warm season as reported by Font *et al.* (1990). Nevertheless, EOF1 becomes again strongly positive during the autumn, reaching a peak by mid-December, in clear agreement with the strengthened shelf-slope jet flowing southwestwards shown in Fig. 9 - f. The temporal structure of EOF2 reveals a principal offshore-directed flow through January-May period and also in late December, coincident with the cold season (October-May) which is characterized by both energetic Mistral winds and Ebro River high discharge rates. Lastly, EOF3 adds clockwise curvature most part of the year (February-September and November). The evident enhancement of the anticyclonic gyre in August (positive EOF3), combined with the onshore-directed flow (negative EOF2) and the reversal of the main current flow (negative EOF1) during that time period, gave rise to a complex circulation scheme, rather similar to the monthly averaged pattern represented in Fig. 9 - d.

In order to define the prevalent wind directions registered at B1, the major and minor variance axes have been determined (Fig. 12 - a). The results show that the main variability occurs along a direction 99º azimuth containing the 54% of the total energy. This is the EOF1 mode, largely aligned with persistent and intense northwesterly mistral winds channeled by the narrow Ebro Valley (Font, 1990). The orthogonal EOF2 mode is oriented 9º clockwise from north and holds the remaining 46% of the variance, capturing mainly the influence of alongshore winds.

Linear correlation coefficients have been computed between the principal components related to the two main wind EOF modes of variability and radar-derived EOF2, since the cross-shelf circulation shown in Fig. 10-c might be presumably driven by strong local winds. The high correlation between the filtered principal components can be readily seen in Fig. 12 (b-c), with a value of 0.47 (0.67) for wind-PC1 (PC2) and radar-PC2, respectively. The results underline that the surface current variability in Ebro Delta can be influenced by wind action, in accordance with Espino et al. (1998), who demonstrated such relationship when winds are strong and steady enough. The higher agreement between both wind-radar PC2 appears to be consistent with Ekman transport to the right of the wind direction. By contrast, northwesterly mistral wind events (PC1) are expected to enforce the prevalent offshore-directed circulation regime (radar EOF2) by increasing the mean speed of the flow.

Equally, the influence of local wind forcing on HF radar EOF1 mode has been assessed (but not shown), with a correlation coefficient of 0.52 (-0.28) for wind PC1 (PC2). This finding highlights the impact of mistral winds on the predominant southwestward flow, by inducing an Ekman veering.

5. Concluding remarks and future work

Since the acquisition of high-quality surface current data remains as a priority for HF radar operators and the research community, a combined quality control (QC) methodology has been applied for a three site standard-range (13.5 MHz) CODAR SeaSonde HF radar network deployed at Ebro Delta (NE Spain). This integrated approach consists of one year-long (2014) real-time web monitoring of nonvelocity-based diagnostic parameters, coordinated with a 6-month (May-October 2014) validation of HF radar data (at both the radial and total vector levels) with independent *in situ* observations from a point-wise current meter installed in B1 buoy, moored within the radar footprint.

The overall stable and accurate performance of Ebro Delta HF radar during 2014, derived from the combined QC-validation approach, suggests that sites were functioning properly and that their APMs were correctly performed and integrated in the data processing. This provides ground truth to examine future radar performances.

The analysis of the monthly averaged spatial patterns of the velocity field shows that the HF radar properly represents basic oceanographic features and recurrent circulation patterns previously observed in the study area, namely: the predominant southwestward flow, the coastal clockwise eddy confined south of Ebro Delta mouth or the Ebro River impulsive-type freshwater discharge. It is also noteworthy that this study has been performed in a low-energy shelf where the surface currents are generally weaker than most of those referenced herein (Lorente *et al*., 2014). The EOF analysis related the flow response to local winds and confirmed that the surface current field evolved in space and time according to three dominant modes of variability, which significantly account for the 46.1% of the variance.

Regarding Ebro Delta study area, active and planned efforts are devoted to an extensive description of a variety of marine processes impacting on the evolution and reshape of the nearshore deltaic area: the wave action eroding exposed wetlands, the sediment transport, the freshwater discharges and buoyancy fluxes (which further complicate water motions in the Ebro Delta) and ultimately the major influence of local wind forcing.

Future works should include the use of verified HF radar data for the rigorous skill assessment of operational ocean circulation systems currently running in Ebro Delta region like IBI (Iberia–Biscay–Ireland) regional system (Sotillo *et al*., 2015), implemented within the frame of MyOcean projects and the Copernicus Marine Environment Monitoring Service (CMEMS). A combined observational and modeling approach would provide a comprehensive characterization of the coastal circulation and benefit from the complementary nature of both systems. HF radar observations improve the model description by resolving low scale processes in areas with significant topographic gradients, whereas model outputs provide a 3-D quantitative picture with vertical resolution that completes the surface radar-derived information when the quality data or the spatiotemporal coverage are poorer.

This integrated strategy might complement and optimize the intense monitoring activity performed around the deltaic coastline through the timely and seamless delivery of high-quality operational products, devoted to support wise decision-making and mitigate anthropogenic hazards in the marine environment. Such products could also provide paramount information on biological connectivity between Ebro Delta marine protected area and other relevant ecological regions in the western Mediterranean Sea.

Acknowledgment

The authors gratefully acknowledge Qualitas Remos Company (partner of CODAR Ocean Sensors) for the useful suggestions and deeply appreciate comments provided during the paper revision process by Dr. Donald Barrick, Dr. Jeffrey Paduan and Dr. Guillaume Charria, which significantly improved the quality of the manuscript. The Spanish Ministerio de Economía y Competitividad supported this study through the OPErational RAdars for research in marine sciences (OPERA) project (CTM2012-33223).

References

Alfonso, M., Álvarez-Fanjul, E., and López, J.D.: Comparison of CODAR SeaSonde HF Radar operational waves and currents measurements with Puertos del Estado buoys, Final Internal Report of Puertos del Estado, 1-32, 2006.

Atwater, D.P., and Heron, M.L.: HF radar two-station baseline bisector comparisons of radial components, Proceedings of IEEE Oceans 2010, Sydney, Australia, pp 1-4, 2010.

Atwater, D.P., and Heron, M.L.: A first approach to SeaSonde quality control, Proceedings of IEEE Oceans 2011, Waikoloa, HI, USA, pp 1-5, 2011.

Barrick, D.E., and Lipa, B.J.: Correcting for distorted antenna patterns in CODAR ocean surface measurements, IEEE Journal of Oceanic Engineering, OE-11: 304–309, 1986.

Barrick, D., Fernandez, V., Ferrer, M.I., Whelan, C., and Breivik, Ø.: A short-term predictive system for surface currents from a rapidly deployed coastal HF radar network, Ocean Dynamics, vol. 62, no. 5, pp. 725–740, 2012.

Chapman, R.D. and Graber, H.C.: Validation of HF radar measurements, Oceanography, 10, N. 2: 76–79, 1997.

Chapman, R.D., Shay, L.K., Graber, H.C., Edson, J.B., Karachintsev, A., Trump, C.L., and Ross, D.B.: On the accuracy of HF radar surface current measurements: intercomparison with ship-based sensors, Journal of Geophysical Research 102 (C8), 18737–18748, 1997.

Codar Ocean Sensors: SeaSonde Diagnostic Files, CODAR Internal Document, May, 2005.

Cosoli, S., Mazzoldi, A., and Gacic, M.: Validation of surface current measurements in the Northern Adriatic Sea from High Frequency radars, Journal of Atmospheric and Oceanic Technology: 27–908, 2010.

Cosoli, S., Gacic, M., and Mazzoldi, A.: Surface current variability and wind influence in the north eastern Adriatic Sea as observed from high-frequency (HF) radar measurements, Continental Shelf Research, 33: 1–13, 2012a.

Cosoli, S., Bolzon, G., and Mazzoldi, A.: A Real-Time and Offline Quality Control Methodology for SeaSonde High-Frequency Radar Currents, Journal of Atmospheric and Oceanic Technology, 29, pp. 1313–1328, 2012b.

Cosoli, S., Licer, M., Vodopivec, M., and Malacic, V.: Surface circulation in the Gulf of Trieste (northern Adriatic Sea) from radar, model, and ADCP comparisons, Journal of Geophysical Research, Vol. 118, 11, pp. 6183-6200, 2013.

Crombie, D.D.: Doppler spectrum of sea echo at 13.56 Mc/s. Nature, 175, 681-682, 1955.

De Paolo, T., and Terrill, E.J.: Skill assessment of resolving ocean surface current structure using compact-antenna-style HF radar and the MUSIC direction-finding algorithm, Journal of Atmospheric and Oceanic Technology, 24: 1277–1300, 2007.

De Paolo, T., Terril, E., and Kirincich, A.: Improving SeaSonde radial velocity accuracy and variance using radial metrics, IEEE Oceans 2015, Genova, pp 1-9, 2015.

Emery, B., Washburn, M.L., and Harlan, J.A.: Evaluating radial current measurements from CODAR high frequency radars with moored current meters, Journal of Atmospheric and Oceanic Technology, Vol. 21: 1259–1271, 2004.

Emery, B.M., and Washburn, L.: Evaluation of SeaSonde Hardware Diagnostic Parameters as Performance Metrics, NOAA IOOS final report, October 2007.

Emery, W.J., and Thomson, R.E.: Data Analysis Methods in Physical Oceanography, Elsevier Science, Amsterdam, 2001.

Espino, M., Sanchez-Arcilla, A., and Garcia, M.A.: Wind induced mesoscale circulation off the Ebro Delta, NW Mediterranean: a numerical study, Journal of Marine Systems, 16, 235–251, 1998.

Font, J., Salat, J., and Tintore, J.: Permanent features of the circulation in the Catalan Sea, Pelagic Mediterranean Oceanography, Oceanologica Acta 9 (vol. sp.), 51-57, 1988a.

Font, J., Salat, J., and Wang, D.P.: Lagrangian and Eulerian observation of inertial oscillations in the shelf break offshore the Ebro River Delta (Catalan Sea, NW Mediterranean), Rapp. Comm. Int. Mer Médit 31: 201, 1988b.

Font, J.: A comparison of seasonal winds with currents on the continental slope of the Catalan sea (Northwestern Mediterranean), Journal of Geophysical Research, Vol 95, NO C2, pp. 1537-1545, 1990.

Font, J., Garcia-Ladona, E. and Gorriz, E.G.: The seasonality of mesoscale motion in the Northern Current of the Western Mediterranean: several years of evidence, Oceanologica Acta, Vol 18, N2, 207-219, 1995.

Garcia, M.A. and Ballester A.: Notas acerca de la meteorología y la circulación local en la región del Delta del Ebro, Invest. Pesquera (now Sci. Mar.) 48 (3), 469-493, 1984.

Gomez, R., Helzel, T., Petersen, L., Kniephoff, K., Merz, C.R., Liu, Y., and Weisberg, R.H.: Real-time quality control of current velocity data on individual grid cells in WERA HF radar, Oceans 2014, Taipei, pp. 1-7, 2014.

Gomez, R., Helzel, T., Merz, C.R., Liu, Y., Weisberg, R.H., and Thomas, N.: Improvements in ocean surface radar applications through real-time data quality-control,

Conference: Current, Waves and Turbulence Measurement (CWTM), IEEE/OES, Florida, USA, March 2015.

Gonella, J.: A rotary-component method for analyzing meteorological and oceanographic vector time series, Deep Sea Research, Part II, 19: 833– 846, 1972.

Graber, H.C., Haus, B.K., Shay, L.K. and Chapman, R.D.: HF radar comparisons with moored estimates of current speed and direction: Expected differences and implications, Journal of Geophysical Research, 102, Nº C8, 18: 749–766, 1997.

Jimenez, J.A., Guillen, J., Sanchez-Arcilla, A., Gracia, V., and Palanques, A.: Influence of benthic boundary layer dynamics on wind-induced currents in the Ebro Delta inner shelf, Journal of Geophysical Research, Vol. 107, C6, 3054, 1-10, 2002.

Kaplan, D.M., Largier, J., and Botsford, L.W.: HF radar observations of surface circulation off Bodega Bay (northern California, USA), Journal of Geophysical Research, 110, C10020: 1-25, 2005.

Kaplan, D.M., and Lekien, F.: Spatial interpolation and filtering of surface current data based on open-boundary modal analysis, Journal of Geophysical Research: Oceans (1978–2012), vol. 112, no. C12, 2007.

Kaihatu, J.M., Handler, R.A., Marmorino, G.O., and Shay, L.K.: Empirical orthogonal function analysis of ocean surface currents using complex and real-vector methods, Journal of Atmospheric and Oceanic Technology, 15, 927–941, 1998.

Kirincich, A. R., de Paolo, T., and Terrill, E.: Improving HF Radar Estimates of Surface Currents Using Signal Quality Metrics, with Application to the MVCO High-Resolution Radar System, Journal of Atmospheric and Oceanic Technology, 29, 1377–1390, 2012.

Kohut, J.T., and Glenn, S.M.: Improving HF radar surface current measurements with measured antenna beam patterns, Journal of Atmospheric and Oceanic Technology, 20: 1303–1316, 2003.

Kovačević, V., Gačić, M., Mancero Mosquera I., Mazzoldi, A., and Marinetti, S.: HF radar observations in the northern Adriatic: surface current field in front of the Venetian Lagoon, Journal of Marine Systems, Volume 51, Issues 1–4, pp 95–122, 2004.

Kundu, P.: Ekman veering observed near the ocean bottom, Jounal of Physical Oceanography, 6, pp. 238-242, 1976.

Kundu, P.K., and Allen, J.S.: Some three-dimensional characteristics of low-frequency current fluctuations near the Oregon coast, Journal of Physical Oceanography 6, 181-199, 1976.

Levanon, N.: Lowest GDOP in 2-D scenarios. IEEE Proceedings, Radar, Sonar Navigation, 147(3): 149–155, 2000.

Lipa, B., Nyden, B., Ullman, D.S., and Terrill, E.: SeaSonde radial velocities: derivation and internal consistency, IEEE Journal of Oceanic Engeneering, 31 (4): 850–861, 2006.

Liu, Y., Weisberg, R.H., and Merz, C.R.: Assessment of CODAR SeaSonde and WERA HF Radars in Mapping Surface Currents on the West Florida Shelf, Journal of Atmospheric and Oceanic Technology, 31, 1363–1382, 2014.

Lorente, P., Piedracoba, S., Soto-Navarro, J., and Alvarez-Fanjul, E.: Accuracy assessment of high frequency radar current measurements in the Strait of Gibraltar, Journal of Operational Oceanography 7 (2), 59–73, 2014.

Lorente, P., Piedracoba, S., Soto-Navarro, J., Ruiz, M.I., Alvarez-Fanjul, E., and Montero, P.: Towards the implementation of a fully operational HF coastal radar network operated by Puertos del Estado, IEEE Oceans 2015, Genova, pp 1-6, 2015a.

Lorente, P., Piedracoba, S., Alvarez-Fanjul, E.: Validation of high-frequency radar ocean surface current observations in the NW of the Iberian Peninsula, Continental Shelf Research 92, pp. 1-15, 2015b.

Lorente, P., Piedracoba, S., Soto-Navarro, J., and Alvarez-Fanjul, E.: A combined QC methodology in Ebro Delta HF radar system: real time web monitoring of diagnostic parameters and offline validation of current data, European Geosciences Union General Assembly (EGU), Vienna, April 2015c.

Marmain, J., Molcard, A., Forget, P. and Barth, A.: Assimilation of HF radar surface currents to optimize forcing in the North Western Mediterranean sea, Nonlin. Processes Geophys., Vol. 21, pp. 659-675, 2014.

Münchow, A. and Chant, R.J.: Kinematics of inner shelf motions during the summer stratified season off New Jersey, J. Phys, Oceanogr., 30, pp. 247-268, 2000.

North, G.R., Bell, T.L., Cahalan R.F. and Moeng, F.J.: Sampling errors in the estimation of empirical orthogonal functions, Mon. Wea. Rev. 110, pp. 699-706, 1982.

Ohlmann, C., White, P., Washburn, L., Terril, E., Emery, B., and Otero, M.: Interpretation of coastal HF radar-derived currents with high-resolution drifter data, Journal of Atmospheric and Oceanic Technology, 24: 666-680, 2007.

Paduan, J.D., Kim, K.C., Cook, M.S., and Chavez, F.P.: Calibration and validation of direction-finding High-Frequency radar ocean surface current observations, IEEE Journal of Oceanic Engineering, 31, N. 4: 862–875, 2006.

Robinson, A.M., Wyatt, L.R., and Howarth, M.J.: A two year comparison between HF radar and ADCP current measurements in Liverpool Bay. Journal of Operational Oceanography, 4: 33–45, 2011.

Roarty, H., Smith, M., Kerfoot, J., Kohut, J., and Glenn, S.: Automated Quality Control of High Frequency Radar Data, IEEE Oceans 2012, pp. 1-7, 2012.

Rypina, I.I., Kirincich, A. R., Limeburner, R. and Udovydchenkov, I. A.: Eulerian and Lagrangian Correspondence of High-Frequency Radar and Surface Drifter Data: Effects of Radar Resolution and Flow Components, Journal of Atmospheric and Oceanic Technology, 31, 945–966, 2014.

Salat, J., Garcia, M.A., Cruzado, A., Palanques, A., Arín, L., Gomis, D., Guillen, J., de León, A., Puigdefàbregas, J., Sospedra, J., and Velásquez, Z.R.: Seasonal changes of water mass structure and shelf-slope exchanges at the Ebro Shelf (NW Mediterranean), Continental Shelf Research 22 (2002), 327-348, 2002.

Schmidt, R.: Multiple emitter location and signal parameter estimation, IEEE Trans. Antennas Propag., 34, pp. 276-280, 1986.

Solabarrieta, L., Rubio, A., Castanedo, S., Medina, R., Charria, G. and Hernández, C.: Surface water circulation patterns in the southeastern Bay of Biscay: New evidences from HF radar data, Continental Shelf Research 74, pp. 60–76, 2014.

Sotillo, M.G., Cailleau, S., Lorente, P., Levier, B., Aznar, R., Reffray, G., Amo-Baladrón, A., and Alvarez-Fanjul, E.: The MyOcean IBI Ocean Forecast and Reanalysis Systems: Operational products and roadmap to the future Copernicus Service, Journal of Operational Oceanography, pp. 1-18, 2015.

Stanev, E.V., Ziemer, F., Schultz-Stellenfleth, J., Seemann, J., Staneva, J. and Gurgel, K.W.: Blending Surface Currents from HF Radar Observations and Numerical Modelling: Tidal Hindcasts and Forecasts, Journal of Atmospheric and Oceanic Technology, Vol. 32, pp. 256-281, 2015.

Taylor, K.E.: Summarizing multiple aspects of model performance in a single diagram, Journal of Geophysical research, 106, pp. 7183-7192, 2001.

Trujillo, D.A., Kelly, F.J., Perez, J.C., Riddles, H.R. and Bonner, J.S.: Accuracy of Surface Current Velocity Measurements Obtained from HF Radar in Corpus Christi Bay, Texas, IEEE/ IGARSS Geoscience and Remote Sensing Symposium, 2: 1179–1182, 2004.

Wyatt, L.: Improving the quality control and accuracy of HF radar currents, IEEE Oceans 2015, Genova, pp. 1-9, 2015.

Yoshikawa, Y., Masuda, A., Marubayashi, K., Ishibashi, M., and Okuno, A.: On the accuracy of HF radar measurement in the Tsushima strait, Journal of Geophysical Research, 111, doi:10.1029/2005JC003232, 2006.

SITE STATUS		
Type	**Parameter**	**Description**
Receiver	MTMP, RTMP	Chassis and board temperatures.
Transmitter	XPHT, XAHT	Chassis and amplifier temperatures.
Transmitter	XAFW, XARW	Forward and reflected powers.
Antenna	SNR1, SNR2, SNR3	Signal-to-Noise ratio at loop 1, loop 2 and the monopole.
Antenna	AMP1, AMP2	Calculated amplitude corrections for loops 1 and 2 to the monopole.
Radial	Number radials / u.t, Range and bearing	Abrupt decrease can be related to a potential malfunction
SYSTEM STATUS		
Parameter		**Description**
Temporal coverage		Data availability (%): areas of poor data return (<50%) are discarded from any analysis.
Evolution of spatial coverage		Monitoring of fluctuations due to day/night cycle. Identification of time-steps of sharp decrease in spatial coverage.
Spatial coverage–VS–Temporal coverage		Verification of the 80%-80% recommended level of data provision.
COS uncertainty metrics (standard deviation of U/V, covariance U/V)		Useful resource, based on fluctuations in the data themselves.

Table 1. Diagnosed parameters used to operationally monitor Ebro Delta HF radar status in real time. The HF radar system's performance is routinely evaluated through the analysis of the below listed indicators on different frequencies (daily / weekly / monthly).

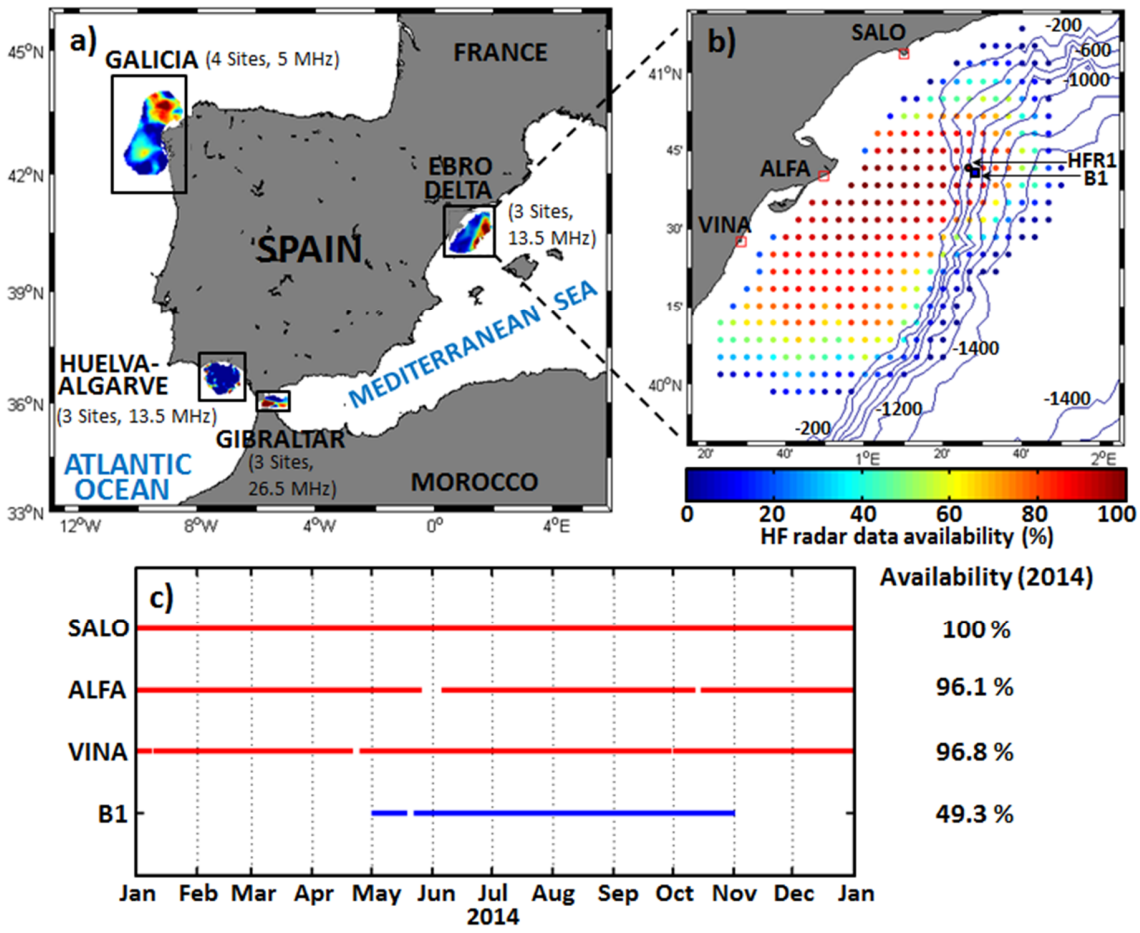

Figure 1. (a) HF coastal radar network currently operated by Puertos del Estado (b) HF radar deployed at the Ebro Delta, composed by three sites: Salou (SALO), Alfacada (ALFA) and Vinaroz (VINA). Colored dots denote the temporal coverage in percent of HF radar surface current total vectors for the entire year 2014. Isobath depths are labeled every 200 m. Location of Tarragona buoy (B1) is marked with filled blue squares. HFR1 denotes the radar grid point closest to B1 position. (c) Time lines of HF radar sites (red) and B1 buoy (blue) current data availability for 2014.

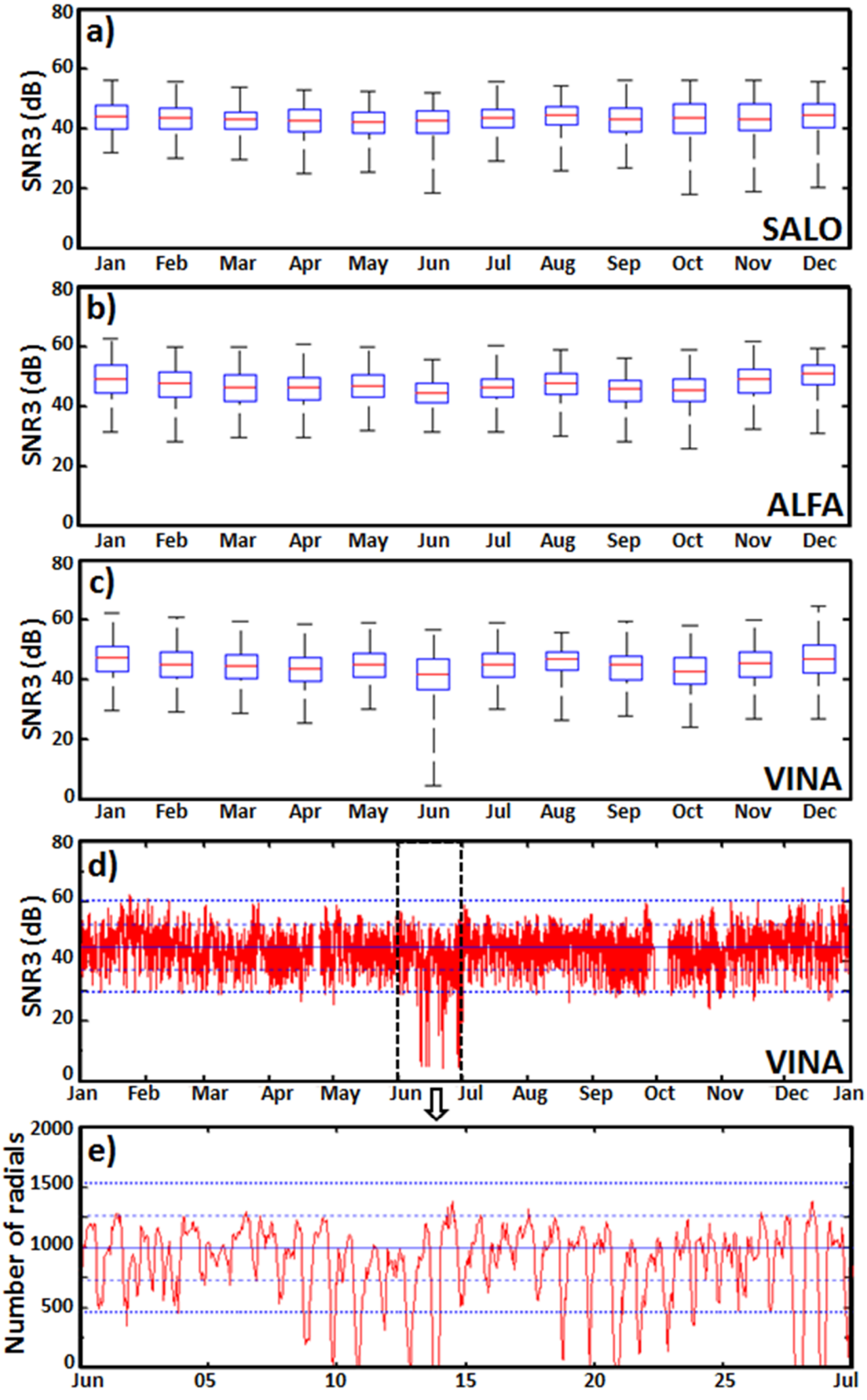
a)
SALO
b)
ALFA
c)
VINA
d)
VINA
e)
SNR3 (dB)
Number of radials
Jan
Feb
Mar
Apr
May
Jun
Jul
Aug
Sep
Oct
Nov
Dec
Jan
05
10
15
20
25
Jul

1

Figure 2. Annual quality control of Ebro Delta radar sites, SALO (a), ALFA (b) and VINA (c), based on monthly boxplots of Signal-to-Noise Ratio at the monopole (SNR3) for 2014. On each box, the central mark is the median, the edges of the box are the 25^{th} and 75^{th} percentiles, and the whiskers extend to the most extreme data points.

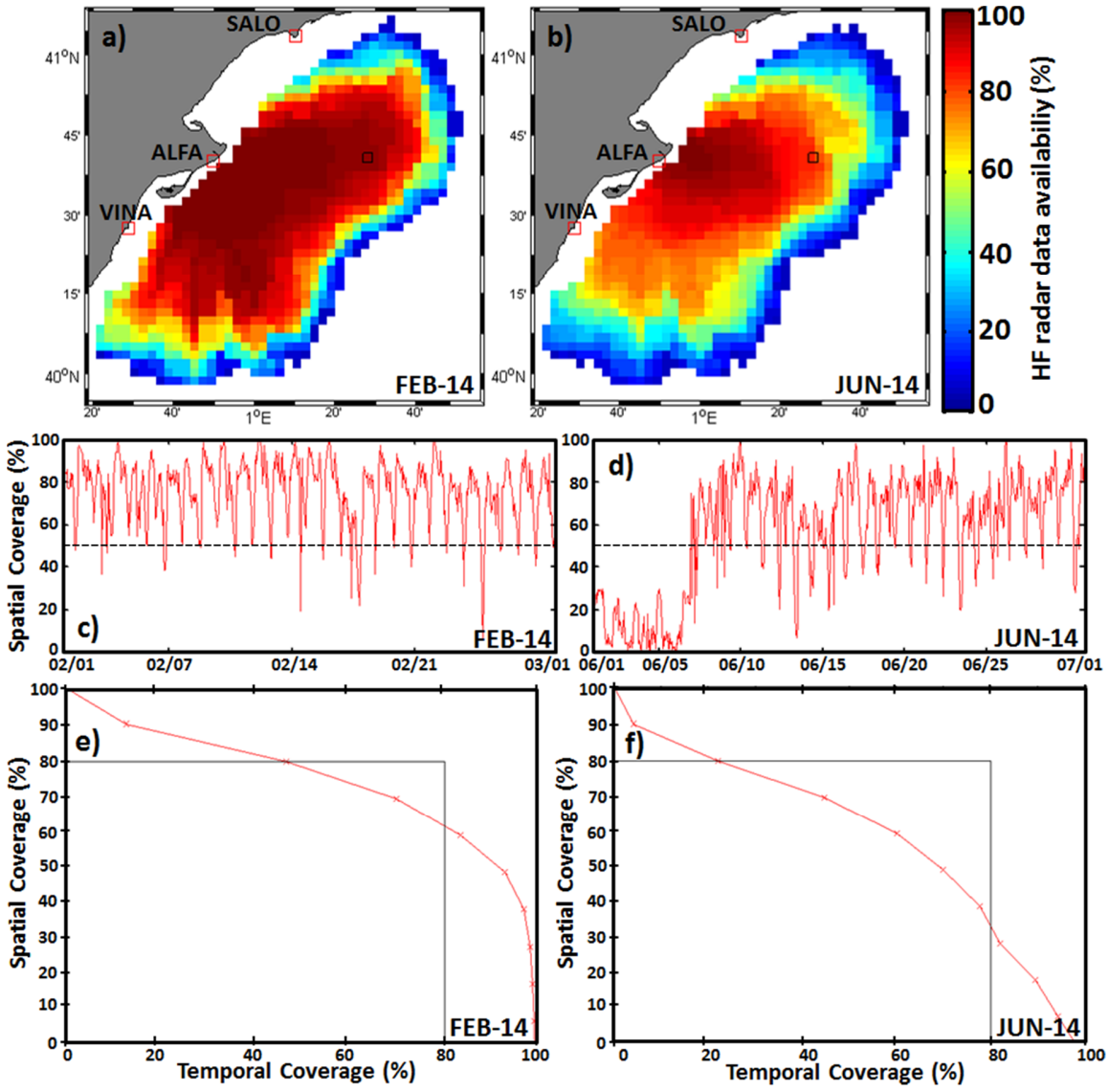

Figure 3. Evaluation of Ebro Delta HF radar system performance on a monthly basis: February (left) and June (right), 2014. A comparative analysis is carried out for the radar data availability (a-b), the temporal evolution of the spatial coverage (c-d) and the relationship between both the spatial and temporal coverage (e-f). The black square represented in (a-b) denotes B1 buoy location.

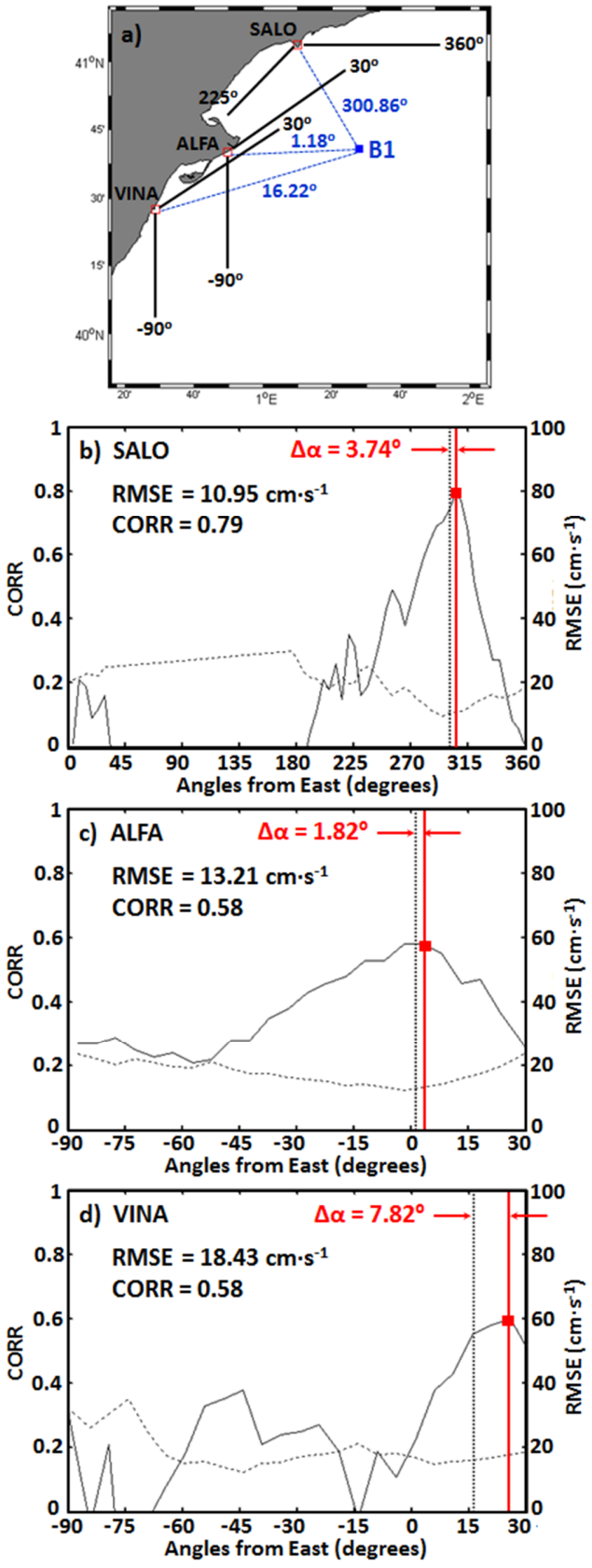
a)
SALO
360°
30°
225°
300.86°
30°
ALFA
1.18°
B1
VINA
16.22°
-90°
-90°
41°N
45'
30'
15'
40°N
20'
40'
1°E
20'
40'
2°E
b) SALO
Δα = 3.74°
RMSE = 10.95 cm·s-1
CORR = 0.79
CORR
RMSE (cm·s-1)
Angles from East (degrees)
c) ALFA
Δα = 1.82°
RMSE = 13.21 cm·s-1
CORR = 0.58
CORR
RMSE (cm·s-1)
Angles from East (degrees)
d) VINA
Δα = 7.82°
RMSE = 18.43 cm·s-1
CORR = 0.58
CORR
RMSE (cm·s-1)
Angles from East (degrees)

1

Figure 4. (a) Angular position of Ebro Delta HF radar sites respect to B1 buoy location. Angle values are measured counter-clockwise from East, indicating arc limits and buoy direction. (b-d) Correlation (solid line) and RMSE (dashed line) between unfiltered radial currents estimated by B1 buoy and those measured by three HF radar sites, SALO (b), ALFA (c), and VINA (d), using calibrated antenna patterns for a 6-month period May-October 2014. Vertical dotted line represents the angular position of B1. Vertical red solid line denotes the angular position of maximum correlation (CORR), which is gathered with the associated RMSE and bearing offset ($\Delta\alpha$) values.

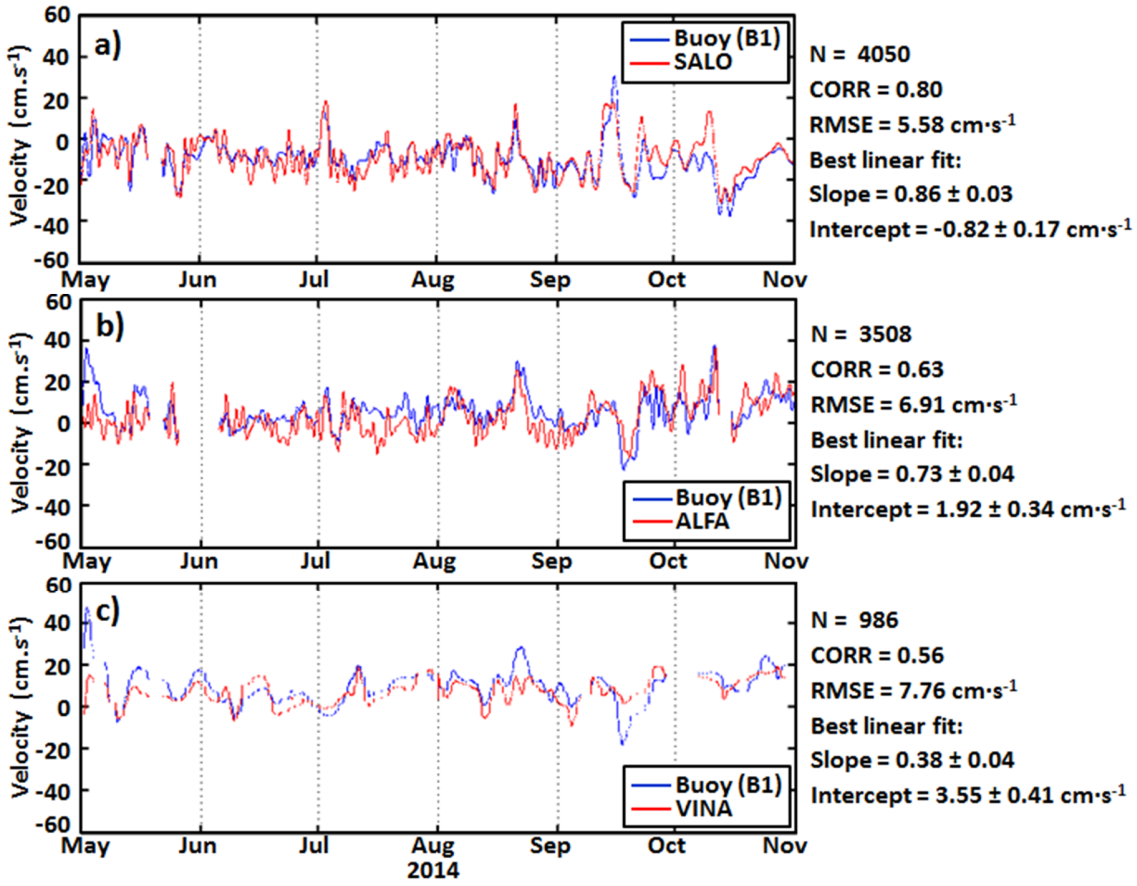

Figure 5. Comparison of low-pass filtered hourly time series (cut-off period of 30 h) of radial currents measured by B1 buoy (blue line) and HF radar sites (red lines): (a) SALO, (b) ALFA and (c) VINA in the range arc point closest to B1 location for a 6-month period May-October 2014, using calibrated antenna patterns. N, slope and intercept represent the number of hourly radial current observations and the results derived from the best linear fits, respectively.

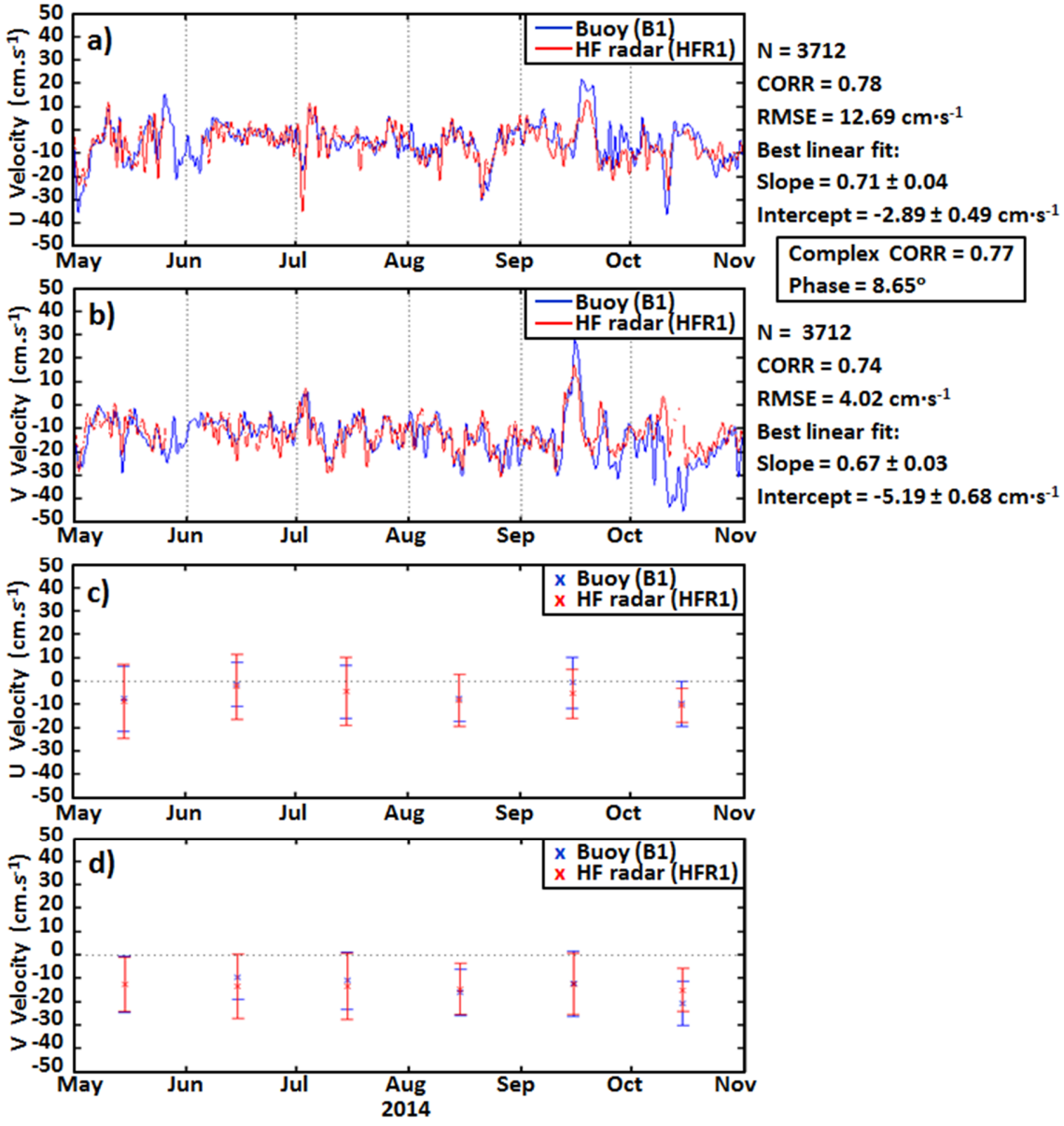

Figure 6. Low-pass filtered (cut-off period of 30 h) hourly time series of zonal (a) and meridional (b) components of total currents measured by B1 buoy (blue line) and HF radar at the closest grid point HFR1 (red line), for a 6-month period May-October 2014. Mean zonal (c) and meridional (d) current velocities, averaged over individual months for both HF radar and B1 measurements, with one standard deviation (error bars represent the 95% confidence interval).

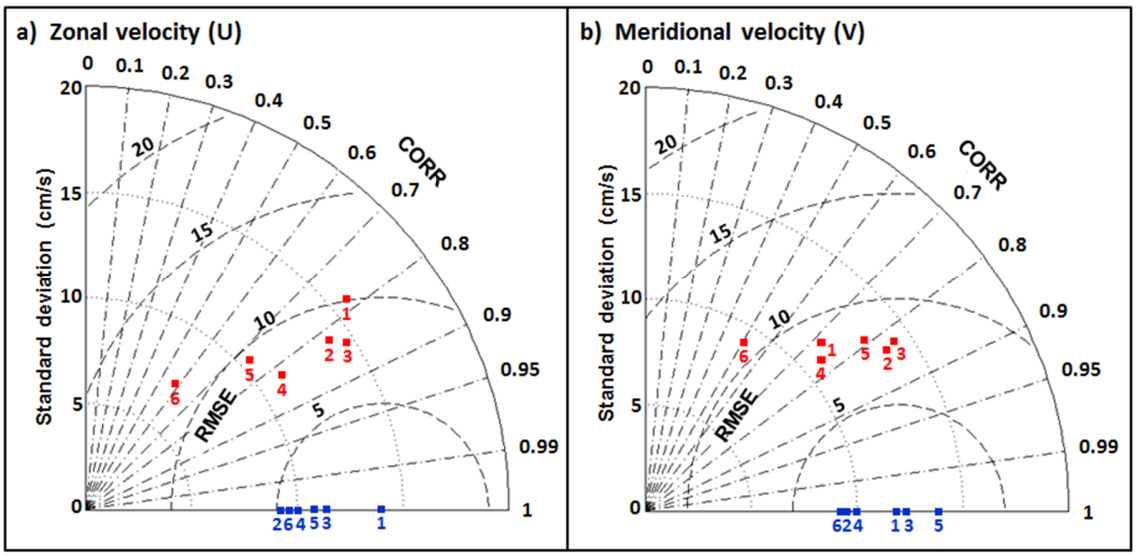

Figure 7. Taylor diagrams, based on the law of cosines, provide a concise statistical summary of how closely unfiltered hourly radar estimations (red filled squares) match with B1 observations (blue filled squares), considered here as the reference points of perfect agreement. Taylor diagrams for zonal (a) and meridional (b) velocity components gather the monthly statistical metrics derived from HF radar – B1 comparison. Sequential numbers refer to individual months of the analyzed period May-October 2014 (1: May; 6: October).

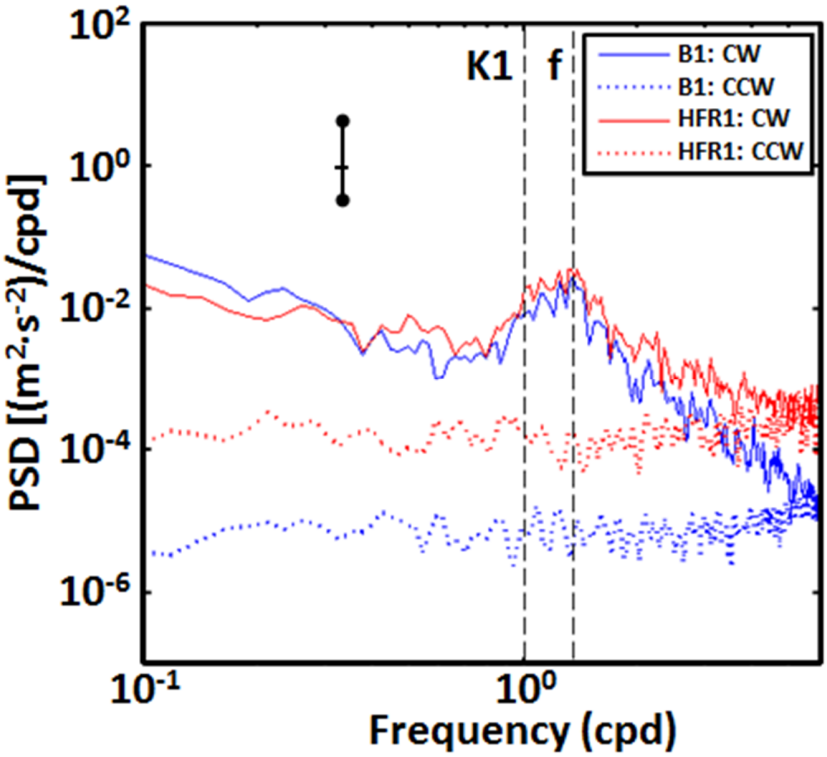

Figure 8. Spectral density of the rotary auto-spectra of B1 buoy (blue) and HF radar at the closest grid point HFR1 (red), performed for a 6-month period May-October 2014 of concurrent records. Clockwise (counter-clockwise) components are represented by solid (dotted) lines. Vertical dashed lines indicate the frequencies of the diurnal constituent (K_1) and the inertial oscillations (f). Error bars indicate the 95% confidence interval.

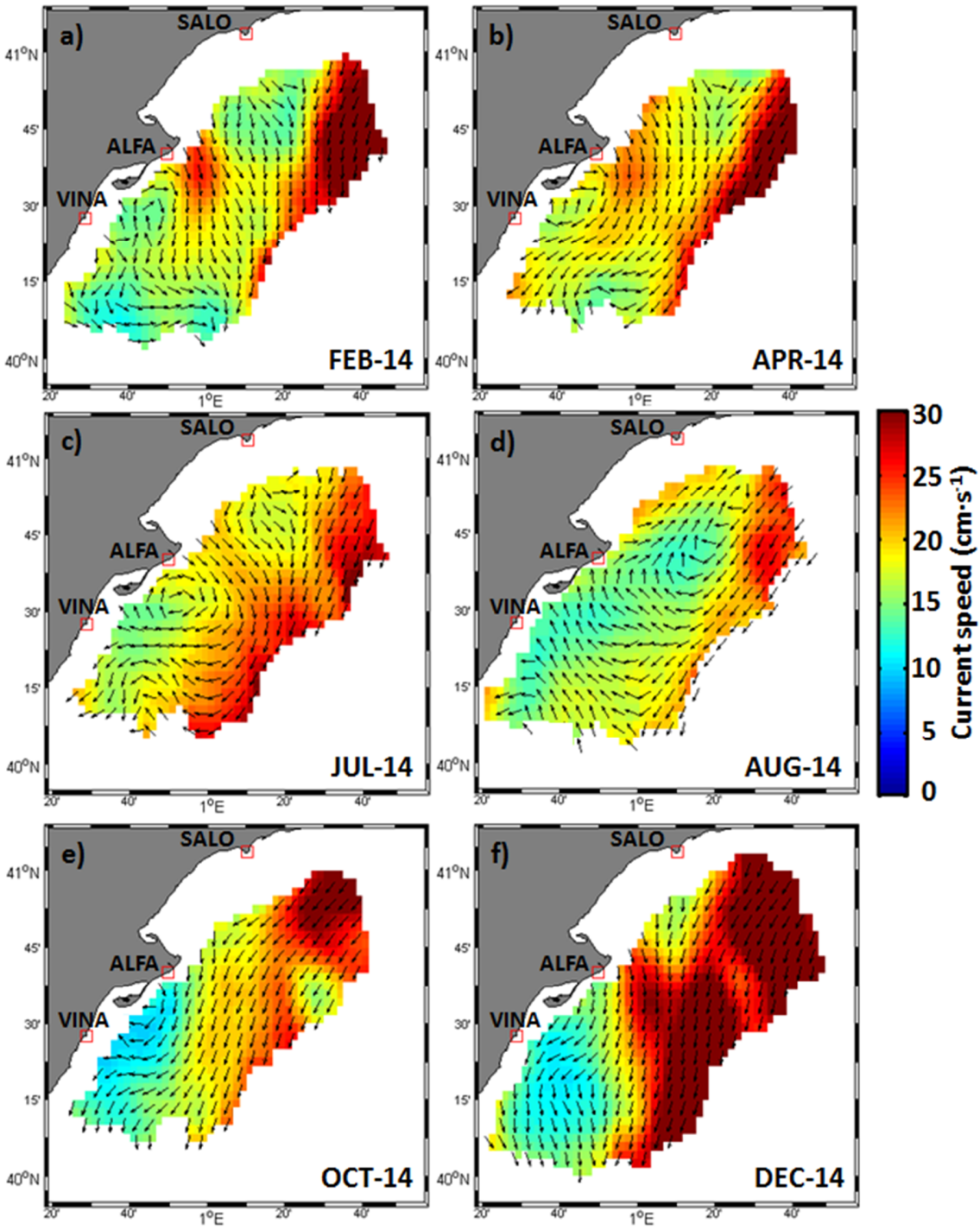

Figure 9. Monthly averaged surface velocity fields, based on unfiltered hourly HF radar current data, for (a) February, (b) April, (c) July, (d) August, (e) October, and (f) December 2014. The study area is not uniformly covered since only radar grid points satisfying a minimum data return of 50% over the monthly record have been considered. Only one grid point of every two is plotted for visualization reasons.

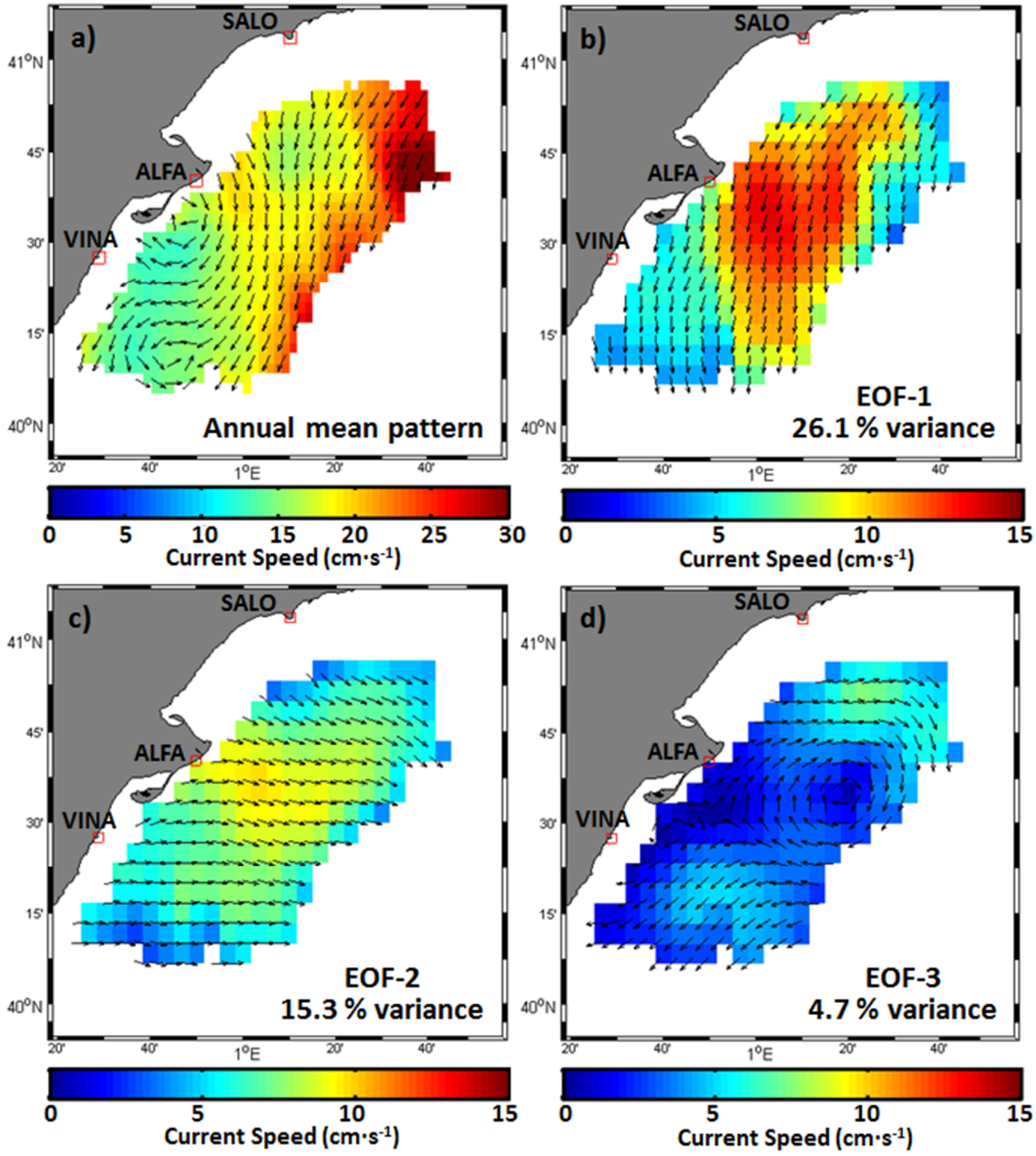

Figure 10. Spatial patterns of the (a) annual mean velocity field and (b) first, (c) second and (d) third EOF dominant modes of unfiltered hourly radar surface currents for 2014. Current vectors were plotted in every second grid point for clarity. Variance explained is indicated in the lower right corner of the corresponding panel.

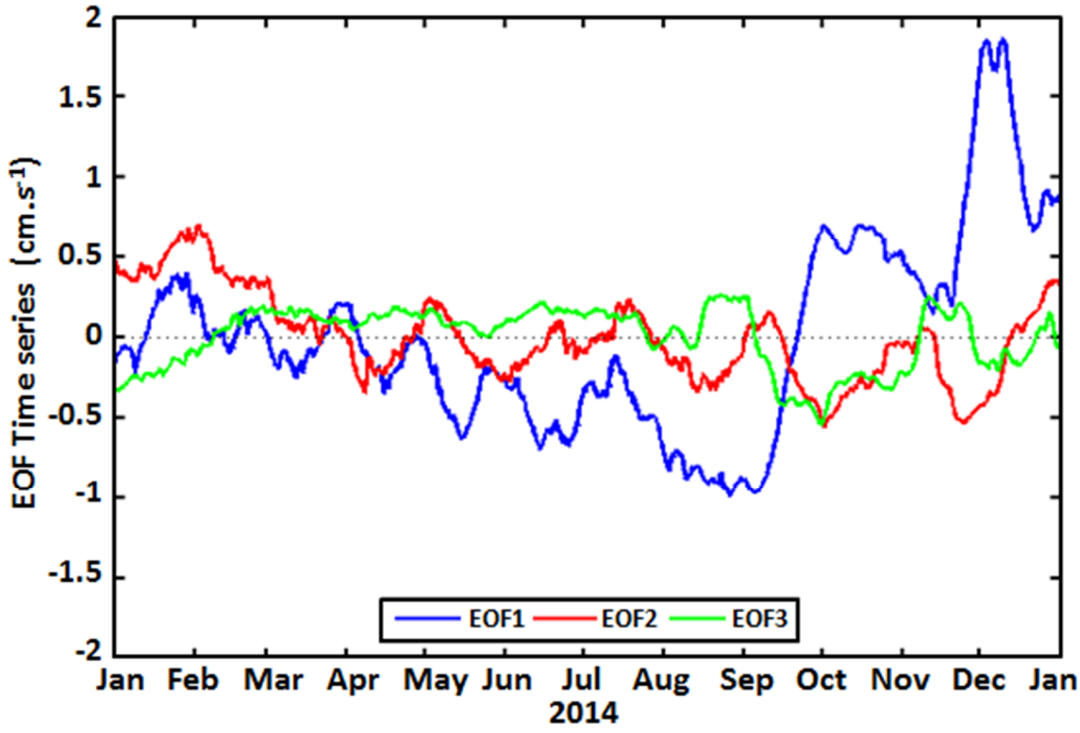

Figure 11. Time coefficients of the first (blue), second (red) and third (green) EOF modes of hourly radar current data set evaluated for the entire year 2014. Time series have been filtered with a 20 day running mean.

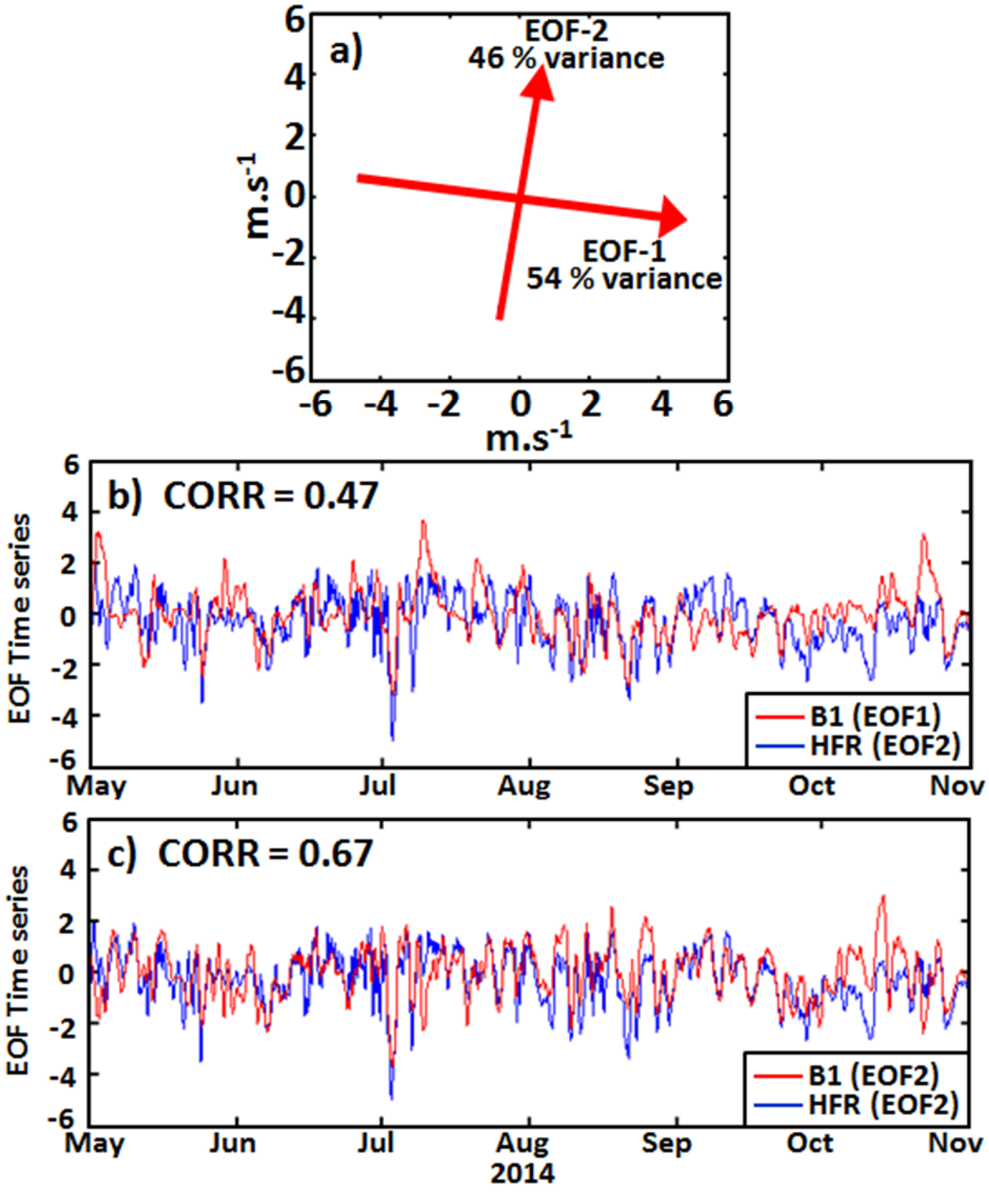

Figure 12. (a) Main axes of variability for hourly wind data registered at B1 buoy. (b) Principal components of the first EOF mode of wind (m/s, in red) and the second EOF mode of radar currents (cm/s, in blue). (c) Principal components of the second EOF mode of wind (red) and the second EOF mode of radar currents (blue). The amplitudes have been normalized by their respective standard deviations and filtered with a 1 day running mean.